ADVANCED ENERGY MATERIALS
www.advenergymat.de

Nanoarchitectonics of Triboelectric Nanogenerator for Conversion of Abundant Mechanical Energy to Green Hydrogen

*Kalyan Ghosh, Christian Iffelsberger, Martin Konečný, Jan Vyskočil, Jan Michalička, and Martin Pumera**

In the present world, the high energy demand rapidly depletes existing fossil fuel reserves, urging the necessity to harvest energy from clean and renewable resources. In this study, the use of a triboelectric nanogenerator (TENG) is shown beyond the conventional practice of use in self-powered electronics, to the production of green hydrogen from renewable mechanical energy. For the first time the use of a magnetic covalent organic framework composite as positive triboelectric material for a contact-separation mode TENG (CS-TENG) in which MXene incorporated polydimethylsiloxane (PDMS) film serves as negative triboelectric material, is demonstrated. A facile way of incorporating micropatterns on the surface of PDMS/MXene film is shown utilizing the advantages of 3D printing technology. The CS-TENG harvests energy from simple mechanical actions such as human handclapping and toe-tapping. The energy from such low-scale mechanical actions is applied for water electrolysis. Scanning electrochemical microscopy is employed to confirm the evolution of hydrogen and oxygen by the harvested electrical energy from mechanical actions. This research is expected to pave the way for producing green hydrogen anywhere, by utilizing the mechanical energy from nature such as raindrops, wind, and the movement of vehicles.

1. Introduction

In the present era, the demand for energy with the rise of the world population and the depletion of fossil fuels directed the supply of energy from green and sustainable energy sources such as solar, wind, and water.[1–3] Green hydrogen is the purest source of energy in the world that can replace fossil fuels with zero-emission to the environment.[4] The use of hydrogen fuel is not only limited to electricity generation but also can be used in industrial sectors for petroleum refining, methanol production, and ammonia production.[5] At present, green hydrogen production from water is mainly based on solar, hydroelectric, and onshore or offshore wind energy sources. On contrary, we see abundant mechanical energy around us in nature from wind, movements of leaves of plants, raindrops, human walking, running vehicles, and waves in the ocean

K. Ghosh, C. Iffelsberger, M. Pumera
Future Energy and Innovation Laboratory
Central European Institute of Technology
Brno University of Technology
Purkyňova 123, Brno 61200, Czech Republic
E-mail: martin.pumera@ceitec.vutbr.cz

M. Konečný
Central European Institute of Technology
Brno University of Technology
Technická 3058/10, Brno 61600, Czech Republic

J. Vyskočil
Center for Advanced Functional Nanorobots
Department of Inorganic Chemistry
Faculty of Chemical Technology
University of Chemistry and Technology Prague
Technická 5, Prague 16628, Czech Republic

The ORCID identification number(s) for the author(s) of this article can be found under https://doi.org/10.1002/aenm.202203476.

DOI: 10.1002/aenm.202203476

J. Michalička
Central European Institute of Technology
Brno University of Technology
Purkyňova 123, Brno 61200, Czech Republic

M. Pumera
Department of Chemical and Biomolecular Engineering
Yonsei University
50 Yonsei-ro, Seodaemun-gu, Seoul 03722, South Korea

M. Pumera
Faculty of Electrical Engineering and Computer Science
VSB – Technical University of Ostrava
17. listopadu 2172/15, Ostrava 70800, Czech Republic

M. Pumera
Department of Medical Research
China Medical University Hospital
China Medical University
No. 91 Hsueh-Shih Road, Taichung 40402, Taiwan

that are often wasted. In 2012, Wang et al. introduced the triboelectric nanogenerator (TENG) that can convert small-scale mechanical energy into electrical energy using the principle of triboelectrification and electrostatic induction phenomenon.[6] In the past decade, researchers explored different materials to harvest vibrational or motion energy for self-powered electronic devices.[7–11] The vast demand for energy beyond self-powered electronics broadens to the conversion of mechanical energy from natural sources toward electrochemical energy via water splitting.[12,13]

So far different models of TENG have been proposed to harvest energy from various forms of motion. The model of TENGs can be classified into four different modes such as a) vertical contact-separation mode, b) sliding mode, c) single-electrode mode, and d) free-standing mode.[6] The vertical contact-separation mode is a simple and effective model to harvest energy from periodic mechanical actions. Such a TENG device consists of two dielectric materials with different surface charge densities, current collectors, and two supporting substrates. A schematic diagram of the vertical contact-separation mode TENG (CS-TENG) is shown in **Figure 1**a. As per the triboelectric series, the relative position of the materials decides which material will lose electrons and which material gain electrons when they come in contact. The materials listed at the top of the series lose electrons and become positively charged while the material at the bottom of the series gains electrons and becomes negatively charged.[6] The higher the difference in their relative position in the triboelectric series, that is, the higher the difference between work functions and surface charges, the better would be the efficiency of TENG. The common negative triboelectric materials are polydimethylsiloxane (PDMS), fluorinated ethylene propylene (FEP), polytetrafluoroethylene (PTFE), located at the bottom of the triboelectric series, and common positive triboelectric materials are human skin, hair, nylon 6, cotton wool, located at the top of the series.[14] To improve the performance of TENG, it is important to explore new materials beyond conventional materials as often found in the triboelectric series.

Covalent organic frameworks (COFs) are evolving crystalline porous polymers in which organic building blocks or units are integrated into a predefined path to form a network structure.[15–18] Since it had been reported in 2005, emerged in several applications, such as gas adsorption,[19] catalysis,[20,21] ion conductors,[22–24] and energy storage,[25,26] due to their evolving structural diversity. COFs are formed through connecting of covalent bonds among light elements, such as C, H, O, N, and B, making them better acceptability than metal–organic frameworks (MOFs) due to the absence of possible toxic metal ions. Recently, MOFs have been explored in TENGs for energy harvesting and sensing applications.[27,28] However, there are limited studies of COFs that have been used as triboelectric materials.[29] The presence of 2D planner covalent sheets of rich π electrons that form an array of π–π network building themselves a potential candidate to be used as positive triboelectric material in TENG.[29,30] The performance of COFs can be enhanced by transforming COF into a magnetic COF composite (Fe_3O_4@COF) through the coating of COF molecules on the magnetic particles. The magnetic material, Fe_3O_4 can allow the Fe_3O_4@COF to provide better triboelectrification toward the negative triboelectric material and better electrostatic induction to the current collector. To the best of our knowledge, the use of Fe_3O_4@COF for a TENG has not been explored yet.

Conversely, the surface properties of conventional dielectric polymer materials can be improved by embedding nano or micro-scale materials into the polymer matrix. The incorporation of nanomaterials into the polymer matrix not only enhances the surface charge density but also provides desirable mechanical properties. In the triboelectric series, PDMS stands almost at the negative end.[31] To develop a high-performance TENG device, recently different inorganic or 2D nanomaterials, such as MoS_2,[32] $BaTiO_3$,[33] MXene,[34–37] carbon nanotubes, and graphene,[38] have been incorporated into the polymer matrix. Among different 2D nanomaterials, transition metal carbides and nitrides, known as MXene,[39,40] have emerged as potential materials for diverse applications such as energy storage,[41–43] gas sensors,[44] and electromagnetic interference shielding.[45,46] MXene is synthesized from the MAX phase, which is represented by the formula $M_{n+1}AX_n$ (n = 1–3) where "M" is transition metal, such as Ti, V, Sc, Cr, and Mo, and "A" is the Group 13 elements, such as Al and Ga, and "X" is C or N. The etching of the "A" layer yields MXene ($M_{n+1}X_nT_x$), where, "T_x" denotes surface terminations (e.g., −F, −O, and −OH). Owing to the presence of electronegative functional groups (−F, −OH) in MXene, its incorporation in familiar PDMS film increases the surface charge density of the PDMS/MXene composite. In addition, the MXene-integrated PDMS film provides good flexibility, robustness, and effortless handling to assemble the TENG device. Although several studies employed PDMS/MXene as a dielectric material for TENG,[34,36,37] there is plenty of room to improve the fabrication methodology and implementation of surface microroughness that gives a higher triboelectric effect. Recently, 3D printing techniques showed countless opportunities to fabricate objects with the desired shape and geometry in a facile way through the decentralized tabletop manufacturing process.[47] The custom design technique provides the desired surface roughness that enhances the triboelectric effect.

Thus, herein we showed a 3D printing-assisted technique to develop microroughness on the PDMS/MXene film. The positive triboelectric material (Fe_3O_4@COF) and negative triboelectric material (PDMS/MXene film) were fabricated via nanoarchitectonics approaches[48] to assemble a CS-TENG. The CS-TENG showed excellent performance to convert mechanical energy into electrical energy. Kelvin probe force microscopy (KPFM) was employed to validate the use of Fe_3O_4@COFs as positive dielectric materials.

We demonstrated the utilization of small-scale mechanical energy from handclapping for the electrolysis of water to the production of hydrogen energy. The scanning electrochemical microscopy (SECM) technique was employed for the non-invasive examination of the hydrogen and oxygen generation and topographic details with a high spatial resolution of the substrates.[49–52] To demonstrate a prototype concept, floor-tiles-shaped supporting substrates were 3D-printed using polylactic acid (PLA) filament, which were assembled to form the CS-TENG for energy harvesting from toe-tapping. Upscaling such smart tiles can be placed at busy bus or train stations to harvest mechanical energy from human walking to green hydrogen fuel.

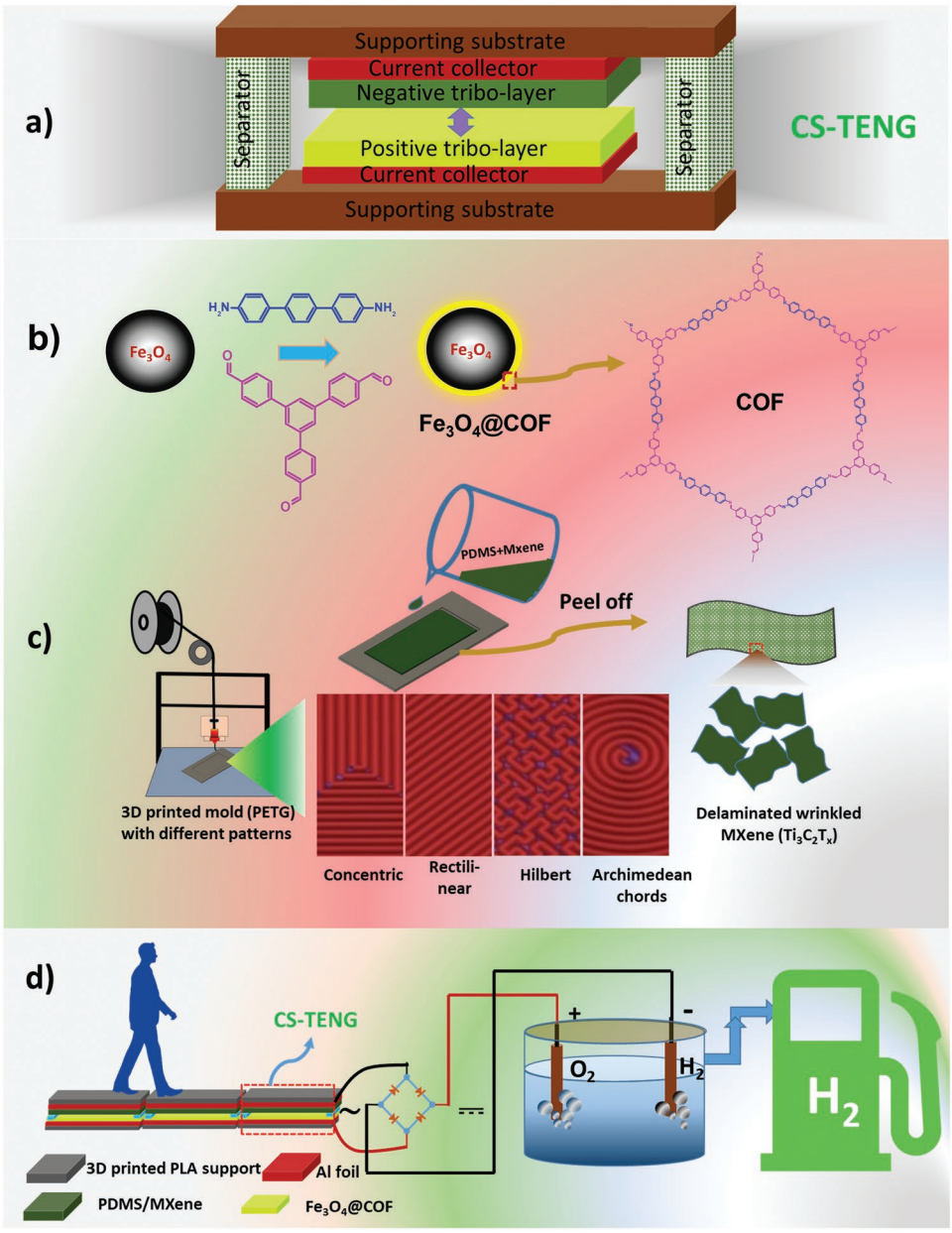

Figure 1. Schematic diagram. a) Contact-separation mode triboelectric nanogenerator (CS-TENG), b) synthesis of magnetic covalent-organic framework (Fe_3O_4@COF) composite, c) fabrication of 3D-printing assisted PDMS/MXene film, and d) conversion of biomechanical energy into green hydrogen fuel.

2. Results and Discussion

The synthesis of positive and negative triboelectric materials and their assembling to fabricate the CS-TENG, and the conversion of mechanical energy from human actions to green hydrogen are presented by schematic diagrams in Figure 1. We separately characterized the negative and positive triboelectric materials followed by electrical characterization of the CS-TENG and conversion of mechanical energy to chemical energy.

2.1. Positive Triboelectric Material

The Fe_3O_4@COF was used as the positive triboelectric material. Three Fe_3O_4@COFs were synthesized only varying the amount of Fe_3O_4 content (100, 300, and 500 mg) keeping the monomer ratio of COF constant. The Fe_3O_4@COFs are denoted as Fe_3O_4@COF-1, Fe_3O_4@COF-2, and Fe_3O_4@COF-3 with increasing content of Fe_3O_4. The Fe_3O_4@COFs exhibit strong magnetic behavior as depicted in Figure S1 and Video S1, Supporting Information. The surface morphology of the

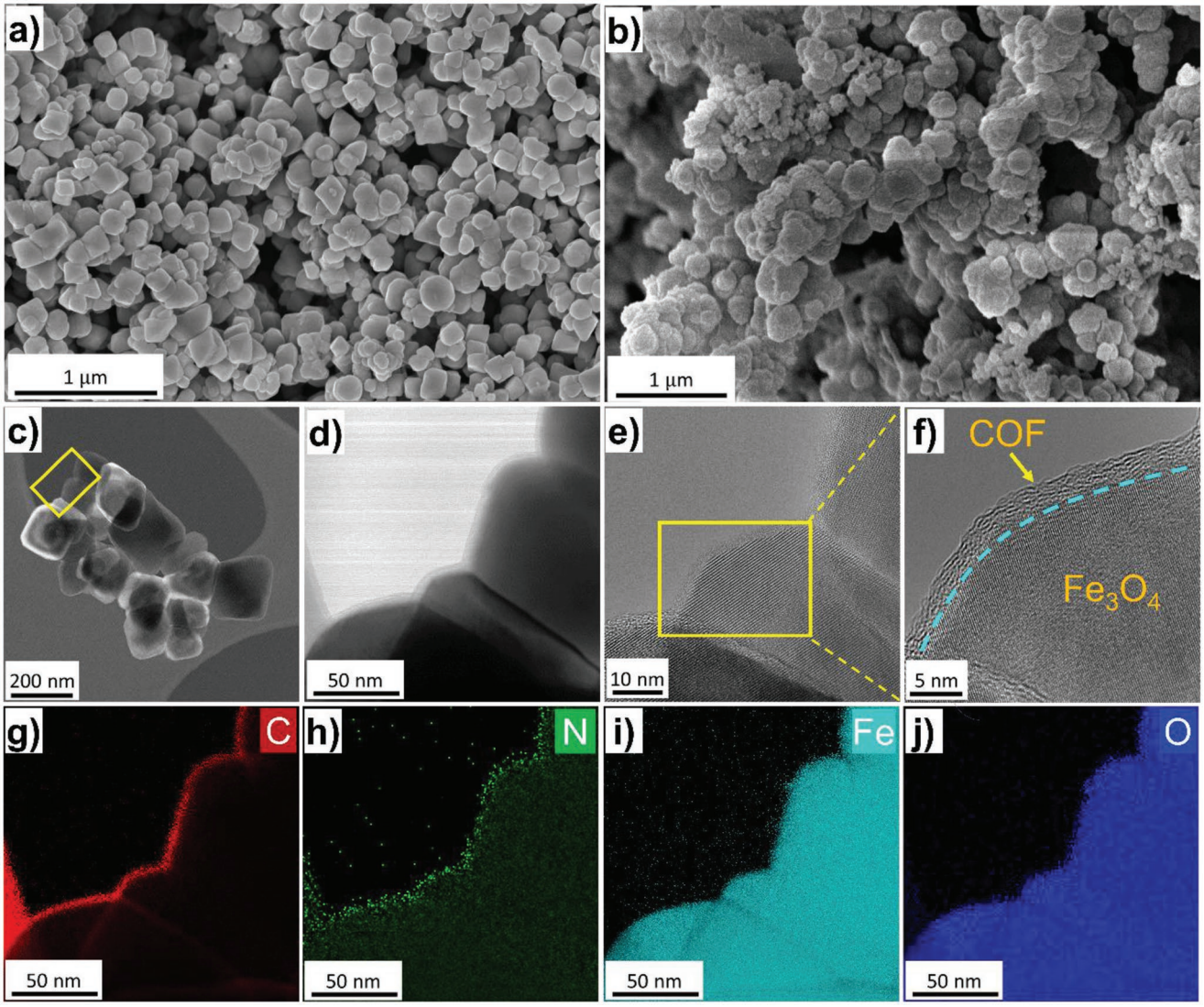

Figure 2. Scanning electron microscopy (SEM) images a) Fe_3O_4 particles, b) Fe_3O_4@COF-2; c,d) scanning transmission electron microscopy (STEM) images and e,f) high-resolution TEM images of Fe_3O_4@COF-2 at different magnifications, and g–j) STEM- energy dispersive X-ray spectroscopy (EDX) elemental maps of C-K, N-K, Fe-K, and O-K corresponding with the sample area shown in d).

Fe_3O_4, COF, and Fe_3O_4@COFs was analyzed using a scanning electron microscope (SEM, Verios). The SEM images of Fe_3O_4 and Fe_3O_4@COF-2 are depicted in **Figures 2**a and 2b, and COF, Fe_3O_4@COF-1, and Fe_3O_4@COF-3 are presented in Figures S2a, S2b, and S2c, Supporting Information, respectively. The Fe_3O_4 microparticles are nearly circular, however, the diameter varies from 100–300 nm. The bare COF shows the porous interconnected granular morphology that originated from the formation of the covalent network of COF building units. The SEM image of Fe_3O_4@COF-2 shows that the Fe_3O_4 microparticles are perfectly coated by the COF creating a core–shell morphology where Fe_3O_4 acts as the core and COF as a shell. Apparently, when the Fe_3O_4 content is low, a higher amount of COF molecules exist in Fe_3O_4@COF-1 (Figure S2b, Supporting Information), while the Fe_3O_4 content is high in Fe_3O_4@COF-3, all the Fe_3O_4 microparticles are not fully covered uniformly (Figure S2c, Supporting Information) by COF. An optimum ratio of Fe_3O_4 and COF was observed for Fe_3O_4@COF-2. Besides, to confirm the core–shell morphology of the Fe_3O_4@COF-2, transmission electron microscopy (TEM) imaging, as depicted in Figures 2c–f, in combination with energy dispersive X-ray (EDX) spectroscopy mapping of the major constituent elements of Fe_3O_4@COF-2 (C-K, N-K, Fe-K, and O-K) in scanning TEM (STEM) mode was performed, as depicted in Figures 2g–j. The high-resolution TEM (HRTEM) images in Figures 2e and 2f show a thin, amorphous coating of the COF layer at single crystal structure of Fe_3O_4 nanoparticles. The STEM-EDX maps then confirm the presence of C and N elements in the shell that originated from the COF molecules. This once again establishes the core–shell structure of Fe_3O_4@COF-2.

To confirm again the formation of COF, X-ray photoelectron spectroscopy (XPS) was carried out for COF, Fe_3O_4, and Fe_3O_4@COF-2 as shown in **Figure 3**a. The wide spectrum of

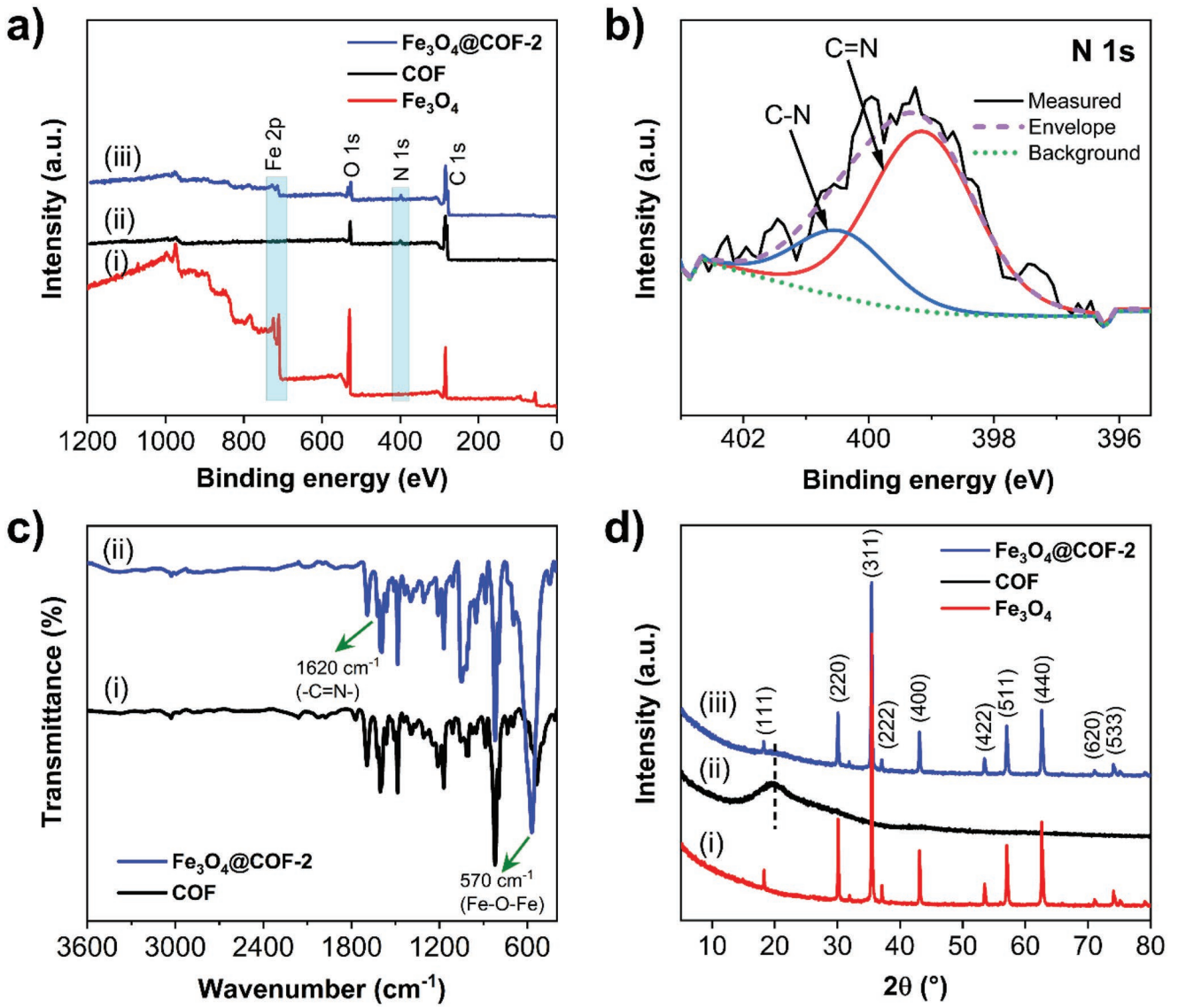

Figure 3. X-ray photoelectron spectroscopy (XPS) (a) survey spectra of i) Fe_3O_4, ii) COF, iii) Fe_3O_4@COF-2, and b) high-resolution core-level deconvolution spectra of N 1s of Fe_3O_4@COF-2; c) Fourier transform infrared spectra of i) COF and ii) Fe_3O_4@COF-2; and d) X-ray diffraction patterns of i) Fe_3O_4, ii) COF, and iii) Fe_3O_4@COF-2.

COF shows the elemental peaks at 285, 400, and 530 eV corresponding to the binding energy of C 1s, N 1s, and O 1s, respectively. The wide spectrum of Fe_3O_4@COF-2 shows an additional peak of Fe 2p along with the core peaks from COF. The high-resolution core level deconvolution of N 1s of Fe_3O_4@COF-2 (Figure 3b) shows the peaks at 399.1 and 400.5 eV corresponding to the binding energy of C=N and C−N bonds alike bare COF (Figure S3a, Supporting Information), confirming the formation of COF on Fe_3O_4. The deconvolution of Fe 2p of Fe_3O_4@COF-2 spectrum (Figure S3b, Supporting Information) shows the peaks at 710 and 724 eV corresponding to Fe $2p_{3/2}$ and Fe $2p_{1/2}$, respectively. Further, the Fourier transform infrared (FTIR) spectra of COF and Fe_3O_4@COF-2 are depicted in Figure 3c. The absence of the N−H stretching vibration band in the range 3200–3400 cm^{-1} confirms that the diamine group of the monomer 4,4″-diamino-p-terphenyl has been completely reacted.[53] The band at 1620 cm^{-1} corresponds to the −C=N− stretching vibration that confirms the formation of the imine-linked COF ring by the reacted monomers.[54] The Fe_3O_4@COF-2 inherits the peak of COF, additionally displaying a strong peak at 570 cm^{-1} corresponding to the Fe−O−Fe vibration of Fe_3O_4.[55] The FTIR study confirms the successful formation of COF and Fe_3O_4@COF-2.

To realize the crystallization behavior of the COF, the X-ray diffraction (XRD) study was carried out for Fe_3O_4, COF, and Fe_3O_4@COF-2 materials as depicted in Figure 3d. The COF shows a wide peak at 2θ of 20°, which states that the COF is in an amorphous phase. The Fe_3O_4 shows the characteristic peaks corresponding to the crystalline planes of (111), (220), (222), (400), (422), (511), (440), (620), and (533) that are well-matched with ICDD cart number 019–0629. The Fe_3O_4@COF-2 shows similar peaks as observed in Fe_3O_4, however, the peak intensity

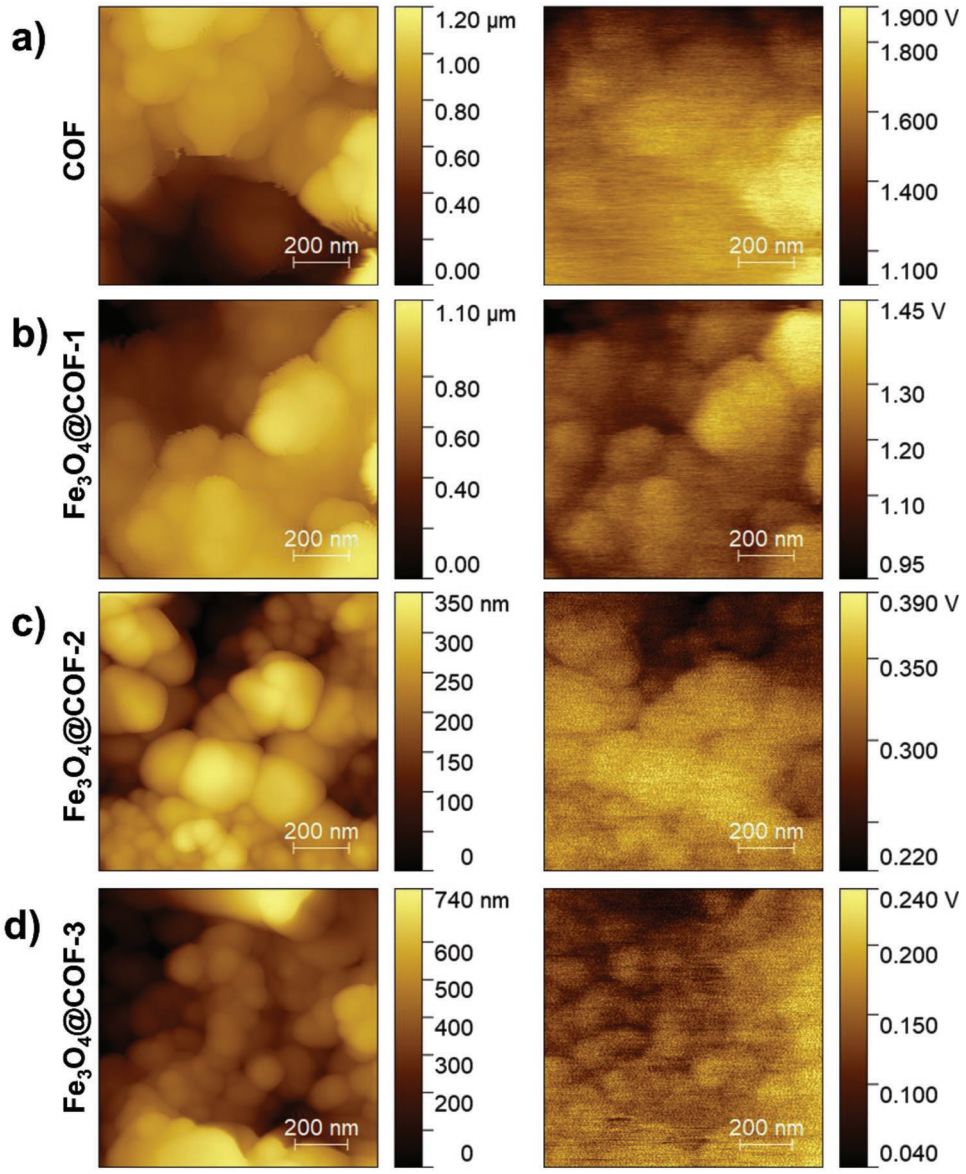

Figure 4. The Kelvin probe force microscopy (KPFM) of a) COF, b) Fe_3O_4@COF-1, c) Fe_3O_4@COF-2, d) Fe_3O_4@COF-3; at left: topography, and at right: KPFM image of contact potential difference (V_{CPD}).

decreased and contain a wide peak from amorphous COF, confirming again the coating of COF on Fe_3O_4 particles.

When the two triboelectric materials come in contact, the work function of the two materials decides which material will lose electrons and which material will accept the electrons. The material that has a comparatively lower work function will lose electrons and act as positive triboelectric material.[56] As the Fe_3O_4@COFs have not been explored previously, KPFM was employed to determine the contact potential difference (V_{CPD}) and work function of the Fe_3O_4@COFs. The captured KPFM topography image and the corresponding V_{CPD} between the KPFM tip and Fe_3O_4@COFs mapping are depicted in **Figure 4**. The statistical analysis (mean profiles) of V_{CPD} for COF and Fe_3O_4@COFs, deduced from Figure 4a–d (right) are presented in Figure S4, Supporting Information). It was observed that the amount of Fe_3O_4 content in the Fe_3O_4@COFs affects the V_{CPD}. The average mean V_{CPD} of COF, Fe_3O_4@COF-1, Fe_3O_4@COF-2, and Fe_3O_4@COF-3 is computed to be 1.59, 1.19, 0.32, and 0.14 V, respectively. Based on the average mean V_{CPD} of the COF and Fe_3O_4@COFs, the work function of the COF and Fe_3O_4@COFs was calculated following Equation (S1), Supporting Information,[57] considering the work function of the KPFM tip (platinum-iridium coated tip of SCM-PIT-V2, Bruker) of 5.5 eV.[58] The work function of the COF, Fe_3O_4@COF-1, Fe_3O_4@COF-2, and Fe_3O_4@COF-3 was deduced to be 3.91, 4.31, 5.18, and 5.36 eV, respectively. The result implies that with increasing the Fe_3O_4 content, the work function increased from Fe_3O_4@COF-1 to Fe_3O_4@COF-3. It is reported that Fe_3O_4 has a work function of 5.32 eV,[59,60] which is close to our measured data of Fe_3O_4@COF-3 with high Fe_3O_4 content. Besides, the

literature-reported data states that the work function of PDMS is 7.59 eV.[61] Thus, the lower work function of Fe_3O_4@COFs confirms that it can be used as positive triboelectric material against PDMS as a negative triboelectric layer.

To fabricate the positive electrode for the CS-TENG device, films of Fe_3O_4@COFs were prepared on the Al surface using a binder as depicted in Figure S5a, Supporting Information. Before coating, to enhance the surface roughness of the film which gives a better triboelectric effect, the Al foil was pressed on a 3D-printed rectilinear patterned surface to imprint the pattern onto it. The surface roughness of the Fe_3O_4@COF-2/Al patterned film was measured using a confocal laser scanning microscope (CLSM, Olympus Lext OLS4100). The optical image in laser mode and topography with false-color mapping in 2D and 3D are shown in Figures S5b, S5c, and S5d, respectively. The colors represent the different heights profile of the patterned film. The Fe_3O_4@COF-2/Al film reports an average surface roughness (measured at 5×5 mm^2 area) of 219 µm along the 9 marked lines as shown in Figure S5c, Supporting Information.

2.2. Negative Triboelectric Material

It is well-known that PDMS is a potential material for negative triboelectric material. However, the surface charge density of the PDMS film can be further improved by incorporating 2D nanomaterials having an electronegative surface functional group.[34,36,38] In this work, to enhance the surface charge density of the PDMS film, MXene $Ti_3C_2T_x$ (T = −F, −OH, =O) was mixed intensively in three different mass ratios (3, 5, and 10 wt%) in the PDMS matrix. The PDMS/MXene composites are denoted as PDMS/MXene-3. PDMS/MXene-5 and PDMS/MXene-10 with increasing weight % of MXene. The MXene and PDMS slurry was cast using customized 3D-printed molds (depth 200 µm) with several patterns such as concentric, rectilinear, Hilbert, and Archimedean chords as integrated with the Prusa slicer software (PrusaSlicer 2.4.2) to embed microroughness on the film surface. To comprehend the type of patterns, a magnified schematic image of the patterns is shown in Figure 1c.

The surface roughness for different engraved micropatterns (concentric, rectilinear, Hilbert, and Archimedean chords) of the PDMS/MXene-5 films were analyzed using the CLSM technique. The optical images of concentric, rectilinear, Hilbert, and Archimedean chords patterns are shown in **Figures 5**a,d,g,k, and their magnified images are presented in Figures 5b,e,h,l, respectively. The magnified images unveiled that the 3D-printed patterns are perfectly engraved onto the film surface. The 2D and 3D CLSM false-color image maps of the topography of all the films are shown in Figure 5c,f,i,m. The 2D and 3D false-color images clearly show the roughness of the engraved patterns. The surface roughness of the films was calculated based on eight different vertical and horizontal lines marked by red, measured at 5×5 mm^2 area. The concentric, rectilinear, Hilbert, and Archimedean chords patterns show surface roughness of 154, 159, 123, and 117 µm, respectively. Apparently, the rectilinear pattern shows the highest surface roughness, and it is noteworthy to mention here that rectilinear patterned film was very easy to peel off from the mold as compared to other patterns.

The detailed XPS analysis of the $Ti_3C_2T_x$ MXene is reported in our previous report.[62] The SEM images at low- and high-magnifications of the delaminated $Ti_3C_2T_x$ are shown in **Figures 6**a and 6b, respectively. It is seen that the $Ti_3C_2T_x$ sheets are crumpled, and a few layers of sheets are stacked together. The TEM image in Figure 6c shows a thin stacked sheets of $Ti_3C_2T_x$. To realize the distribution of $Ti_3C_2T_x$ in the PDMS matrix, the SEM-EDX mapping was carried out for all the PDMS/MXene films. The mapped area and elemental mapping of Ti, F, C, and Si of PDMS/MXene-3, PDMS/MXene-5, and PDMS/MXene-10 films are depicted in Figures 6d–f, respectively. The maps of Ti and F indicate the distribution of $Ti_3C_2T_x$ MXene in the PDMS matrix. Comparing all the films, it is evident that PDMS/MXene-5 shows well distribution of MXene in the matrix. The dense spots that are observed in the map of Ti and F depict the agglomeration of several $Ti_3C_2T_x$. Except for the dense spotted area, the $Ti_3C_2T_x$ are well dispersed in the PDMS matrix. However, at lower MXene content in PDMS/MXene-3 film, the Ti and F signals are low, whereas for higher MXene content in PDMS/MXene-10 film, the bright spots of Ti and F evident that MXene particles are agglomerated and connected at the most region of the film matrix. The cross-section image of the film is shown in Figure S6, Supporting Information, which states the film has a thickness of ≈200 µm.

The electrical resistivity of the composite films was measured using a four-probe station following the van der Pauw method. The PDMS/MXene-3, PDMS/MXene-5, and PDMS/MXene-10 films show the average surface sheet resistivity of 2130×10^3, 216.4×10^3, and 190.22×10^3 Ω sq^{-1}, respectively. As $Ti_3C_2T_x$ is a conductive material, the diminution of surface resistivity was most obvious with increasing of $Ti_3C_2T_x$ concentration.

2.3. Conversion of Mechanical Energy into Electrical Energy

A schematic of the cross-sectional view of the assembled CS-TENG is shown in **Figure 7**a. The device is constructed using the PDMS/MXene as negative and Fe_3O_4@COF as positive triboelectric layers. Al foil was used as a current collector and 3D-printed PLA was used as supporting substrates for both layers. We selected 3D-printing technology to construct the supporting substrate because it provides easy fabrication of any shape and geometry. The supporting substrate was designed in a way that aided to assemble the CS-TENG device as a prototype model of the smart tile. A reciprocal linear actuator was used to hit the top plate of the CS-TENG allowing periodic contact and separation between the triboelectric layers. The triboelectric layers are separated by a distance of ≈2 mm using two pieces of polyurethane foam. The whole device remains neutral at the beginning (Figure 7b-I). While the actuator hits on the top plate, the triboelectric layers of Fe_3O_4@COF and PDMS/MXene film come in contact. At the pressing cycle, when the Fe_3O_4@COF film contacts the PDMS/MXene film, the MXene/PDMS film attracts electrons from Fe_3O_4@COF and its surface becomes negatively charged, while the surface of Fe_3O_4@COF becomes positively charged (Figure 7b-II). At the releasing cycle, when the Fe_3O_4@COF film moves away, the negative charge of PDMS/MXene film induces a positive charge on the attached Al electrode through the electrostatic induction effect.

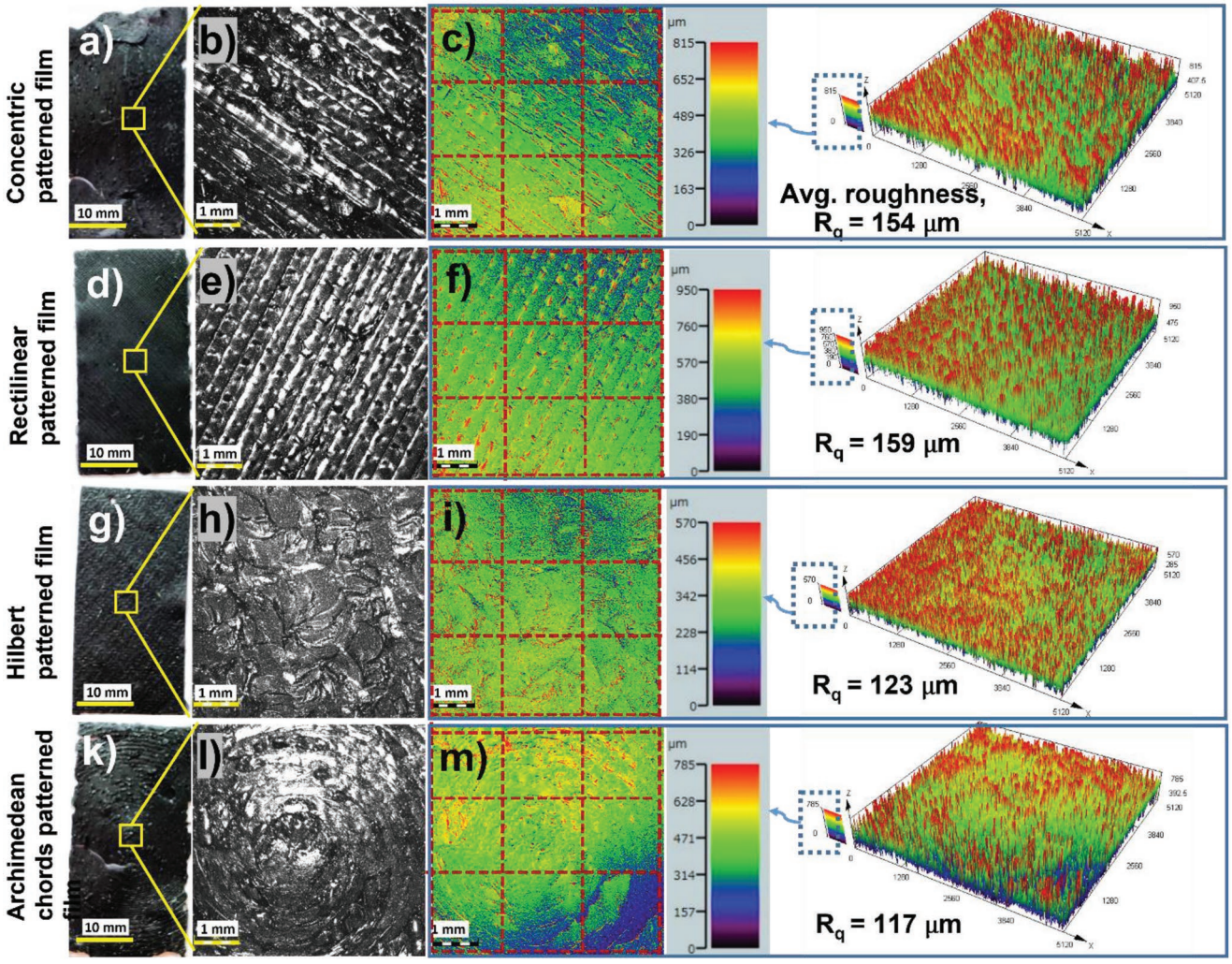

Figure 5. Confocal laser scanning microscope (CLSM) images: a,d,g,k) at low- and b,e,h,l) high-magnification, c,f,i,m) at left: 2D and at right: 3D false-color mapped images for the topography of concentric, rectilinear, Hilbert, and Archimedean chords patterned PDMS/MXene-5 films, respectively.

Similarly, Fe_3O_4@COF film induces the negative charge to the attached Al electrode. Thus, free electrons flow from negatively charged Al to positively charged Al, giving an output signal (Figure 7b-III). When the two plates are completely separated, the surface charge will be fully screened out and no electric signal will be observed (Figure 7b-IV). In the subsequent pressing cycle, while the two plates come in contact, the electrons will flow back, and a reverse electric signal appeared (Figure 7b-V). Such periodic contact separation causes two conditions, open-circuit potential (V_{oc}) and short-circuit current (I_{sc}) that are explained in Supporting Information (Equations (S2)–(S5), Supporting Information). The periodic hammering generates alternate current signals as shown in Figure 7b-VI.

The output performance of PDMS/MXene films was optimized by varying the weight percentage of $Ti_3C_2T_x$ (0, 3, 5, and 10 wt%). The addition of $Ti_3C_2T_x$ MXene into the PDMS matrix enhances the surface and bulk capacitive properties.[36] The V_{oc} and I_{sc} of bare PDMS, PDMS/MXene-3, PDMS/MXene-5, and PDMS/MXene-10 film for the rectilinear engraved pattern at a contact frequency of 10 Hz with a contact force of 2.8 N were recorded as depicted in **Figures 8**a and 8b, respectively. It was observed that with increasing the concentration of $Ti_3C_2T_x$ in the PDMS matrix, the V_{oc} and I_{sc} were increased from 0 to 5 wt%. Apparently, the PDMS/MXene-5 displays 3.5 times higher peak-to-peak $V_{oc(pk\text{-}pk)}$ of ≈146 V and $I_{sc(pk\text{-}pk)}$ of ≈32 μA than the bare PDMS film at a contact frequency of 10 Hz. The higher performance of PDMS/MXene film can be attributed to the presence of electronegative surface functional groups (−F, −OH) in $Ti_3C_2T_x$ that increase the negative surface charge density of the PDMS/MXene films. Moreover, the high conductivity of $Ti_3C_2T_x$ reduces the electrical resistance of the composite film. In addition, $Ti_3C_2T_x$ increases the relative permittivity of the composite which results in higher performance.[34] However, 10 wt% of $Ti_3C_2T_x$ concentration in the PDMS matrix showed lower performance as compared to 5 wt% composite films. At the high concentration of $Ti_3C_2T_x$ (10 wt%), the 2D particles form a conductive path and attenuate the dielectric properties of the PDMS.[36,37] This results in less charge build-up at the film surface because of the leaking of charge from the conductive PDMS/MXene film to adjacent Al. As the 5 wt%

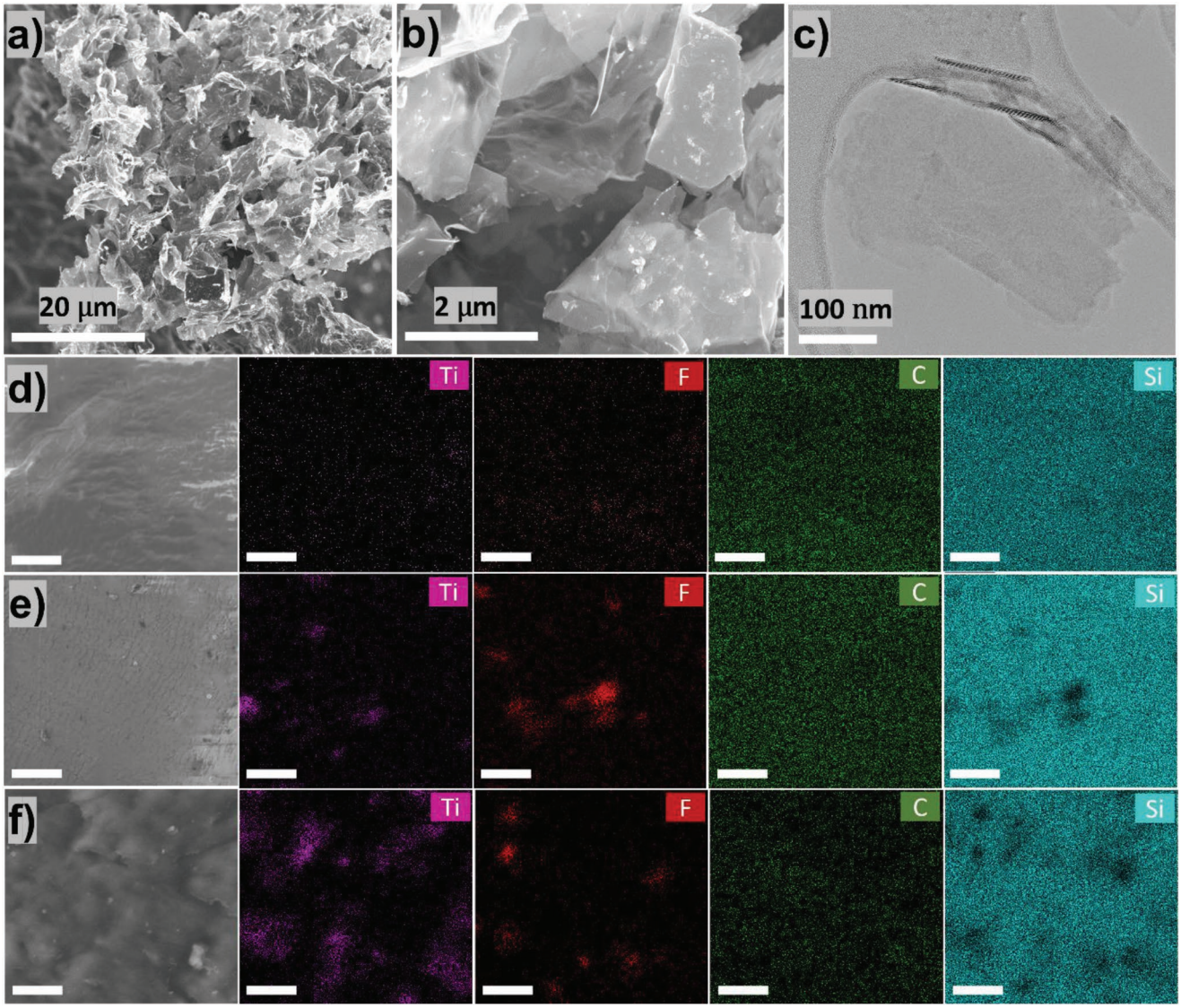

Figure 6. Scanning electron microscopy (SEM) images a) at low-, b) at high-magnifications; and c) a transmission electron microscopy image of $Ti_3C_2T_x$. SEM-energy dispersive X-ray spectroscopy (EDX) mapping depicting the mapped area, and elemental mapping of Ti-K, F-K, C-K, and Si-K of d) PDMS/MXene-3, e) PDMS/MXene-5, and f) PDMS/MXene-10 films, respectively. d–f) scale bar =10 µm.

$Ti_3C_2T_x$ concentration gives the highest performance we selected this composition of film for further analysis in the following sections. It was observed that the potential differences between the electrodes in the pressing and releasing cycles are not symmetric for all cases. This can be attributed to the occurrence of several effects like contact electrification, electrostatic induction, and charge redistribution between the electrodes that make the different intensities of alternate signals.

Further, the effect of contact frequency on the V_{oc} and I_{sc} was also determined by systematically increasing oscillation frequency from 6 to 10 Hz as shown in Figures 8c,e, respectively. It was found that with increasing the contact frequency, the V_{oc} and I_{sc} increased. This can be explained by the proposed model presented by Yang et al,[63] where it has been shown that the speed of the top plate of CS-TENG affects the output performance. The output voltage and current increase monotonically with increasing the speed of the hitting layer, that is, with increasing the contact frequency as observed in Figure 8c,e. The magnified signals of V_{oc} and I_{sc} against time at the contact frequency of 10 Hz are depicted in Figures 8d,f, respectively. The magnified plots clearly show the sinusoidal waveform of the voltage and current during releasing and pressing cycles. Besides, the AC signals were rectified to DC signals connecting a bridge rectifier to the CS-TENG output terminals. The DC signals of V_{oc} and I_{sc} are depicted in Figures 8g,h, respectively, which shows that the CS-TENG generates a rectified V_{oc} of ≈100 V and I_{sc} of ≈19 µA at the oscillation frequency of 10 Hz. It is to be noted that the contact-separation process is instantaneous and continuous. After a contact-separation cycle, when the two electrodes come in contact in the next cycle, the number of electrical charges flowing back is not equal to the previous cycle and thus resulted in small discrepancies in the amplitude of the peaks.

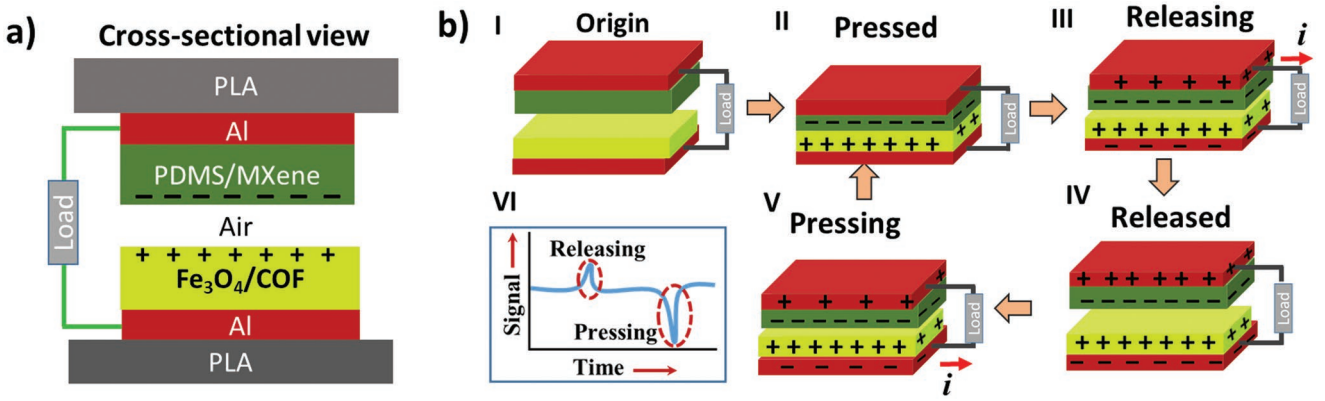

Figure 7. a) Schematic of a cross-sectional view of the CS-TENG, b) I–V) the different charge transfer at states of contact-separation, and VI) schematic of obtained alternate current response from a contact-separation cycle.

Moreover, we compared the output electrical performance of different 3D-printed engraved patterns of concentric, rectilinear, Hilbert, and Archimedean chords on the surface of PDMS/MXene-5 films as shown in **Figure 9**a,b. Among them, the film with a rectilinear pattern provides the highest $V_{oc(pk\text{-}pk)}$ of ≈146 V and I_{sc} of ≈32 µA at the contact frequency of 10 Hz. This result is attributed to the higher surface roughness of the rectilinear pattern as we found in CLSM measurement. Based on the comparison results of V_{oc} and I_{sc}, the rectilinear patterned film was selected for further study. Besides, the output performance of Fe_3O_4@COFs-based CS-TENGs was compared with bare COF and Fe_3O_4 at the contact frequency of 6 Hz using PDMS/MXene-5 rectilinear film as a negative triboelectric layer as depicted in Figure 9c. The Fe_3O_4@COF-2 shows the highest output performance. The average $V_{oc(pk\text{-}pk)}$ of COF, Fe_3O_4@COF-1, Fe_3O_4@COF-2, Fe_3O_4@COF-3, and Fe_3O_4 are deduced to be 28, 35, 69, 35, and 15 V, respectively. From the KPFM measurement, it was found that work function increased from bare COF to Fe_3O_4/COF-3 with increasing content of Fe_3O_4. As explained previously, the higher the difference in work function between positive and negative electrodes, the higher would be the electrical performance. Herein, bare COF shows the highest difference in work function with respect to the PDMS film, however, it shows lower performance than the Fe_3O_4@COFs. The Fe_3O_4@COF-2 displays two times higher performance than the bare COF. This can be attributed to the uniform coating of COF on Fe_3O_4, which plays a crucial role to transfer the triboelectric charge to the current collector. It was observed that, during contact-separation cycles, friction between the top and bottom electrodes detached COF particles partiality from the Al surface and stuck onto the PDMS/MXene-5 film. This hindered to materialize of the sole performance of COF molecules. On the contrary, Fe_3O_4@COF-2 shows a good film formation on the Al surface due to the presence of core Fe_3O_4 particles, which attached well to the film surface and are stable over long cycles of contact separation. Although Fe_3O_4@COF-5 gives a good film formation, however, due to its higher work function, it shows lower performance than Fe_3O_4@COF-2. The core performance of Fe_3O_4 particles was the least because of its high work function and absence of the dielectric COF layer. Hence, we select Fe_3O_4@COF-2 for further study. We calculated the power density of the CS-TENG varying the external load resistance from 1 to 10^5 Ω, which is depicted in Figure 9d. With increasing the external load, the current density decreased, and the power density increased to 8.04 µW cm^{-2} at the load of 10^5 Ω.

Further, the output performance of the device was recorded under different mechanical actions, such as toe-tapping and handclapping, as demonstrated in Videos S2 and S3, Supporting Information, respectively. Continuous toe-tapping and handclapping generate average $V_{oc(pk\text{-}pk)}$ of 40 and 55 V, as shown in Figures 9e,f, respectively. Three CS-TENG devices are connected in parallel to demonstrate the energy conversion from walking as shown in Video S4, Supporting Information. The model can be extended to a large area like a busy train station to harvest energy from human walking.

2.4. Conversion of Mechanical Energy into Chemical Energy via Water Splitting

We present the conversion of mechanical energy as a renewable energy source to produce green hydrogen. Since the amount of produced hydrogen scales with the current, based on the output performance of the CS-TENG (area 20 × 40 mm^2), the occurrence of hydrogen and oxygen were evaluated above two 50 µm diameter Pt microelectrodes (generation electrodes, cathode/anode) with SECM as a detection method. The microscopic information was generated by recording an amperometric current at the SECM probe (collector electrode), which was typically a disc-shaped Pt ultra-microelectrode (UME, 25 µm diameter). For the detection of the generated hydrogen and oxygen, the substrate generation/tip collection (SG/TC) mode was used.[64] In this mode, the substrate (Pt cathode/anode) generated species were collected at the UME and the signal intensity correlates with the concentration of generated species. The hydrogen and oxygen were detected at UME using reduction and oxidation reactions that were indicated by high positive or high negative currents, respectively.

The schematic representation of the experimental setup is depicted in **Figure 10**a. The application of an electrical potential between two electrodes results in a hydrogen evolution reaction (HER) (Equation (1)) at the cathode and an oxygen evolution reaction (OER) (Equation (2)) at the anode.

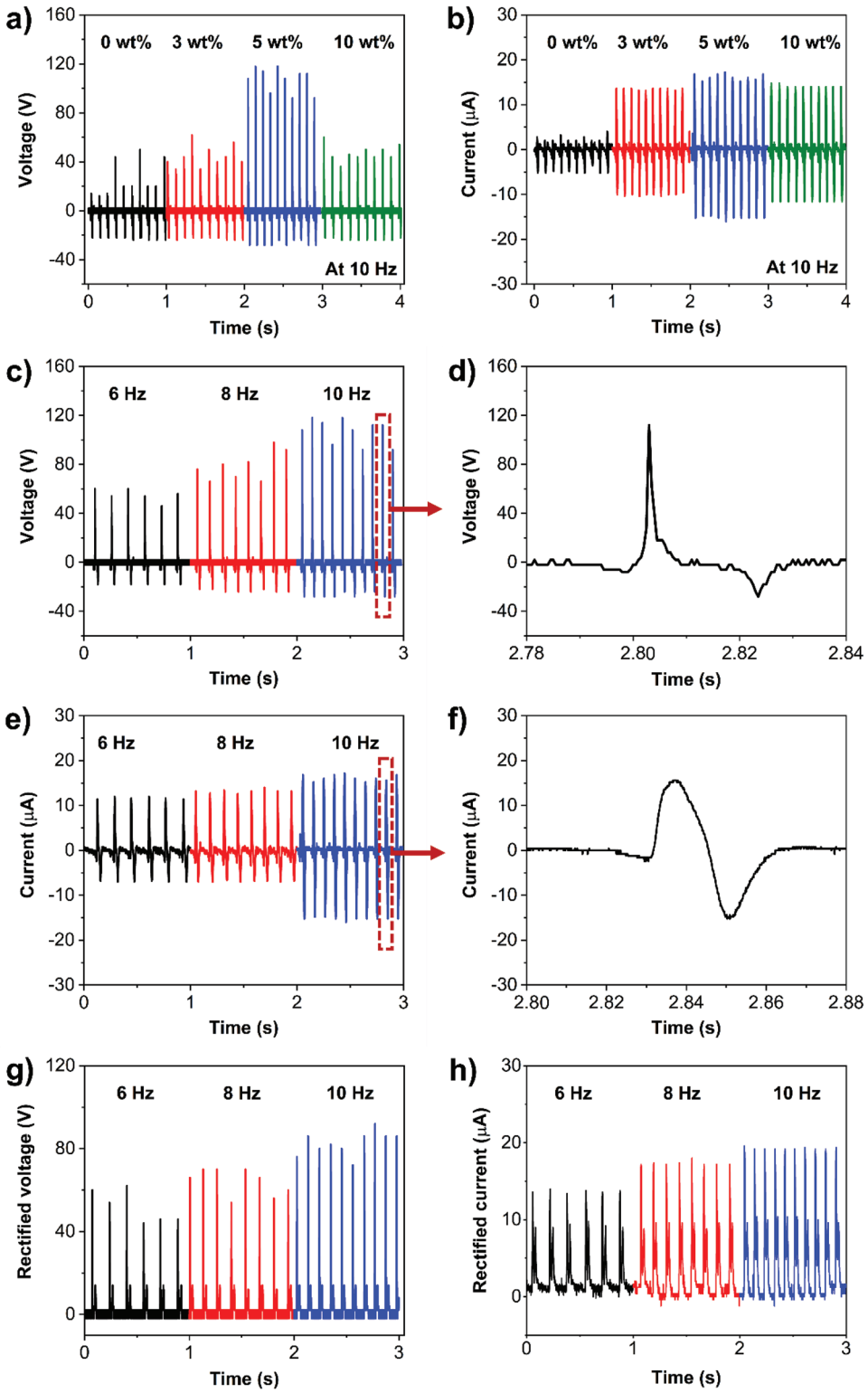

Figure 8. Variation of a) open-circuit voltage (V_{oc}) and b) short-circuit current (I_{sc}) with $Ti_3C_2T_x$ concentration; variation of c) V_{oc} and e) I_{sc} with contact frequency, magnified plots of d) V_{oc} and f) I_{sc} against time; rectified g) V_{oc} and h) I_{sc} at different contact frequencies while connected by a bridge rectifier with the CS-TENG terminals. Contact force = 2.8 N.

$$2H_3O^+ + 4e^- \rightarrow H_2 + 2H_2O \quad (1)$$

$$2H_2O \rightarrow O_2 + 4H^+ + 4e^- \quad (2)$$

To obtain continuous evolution of H_2 and O_2 applying the output voltage of CS-TENG, a bridge rectifier was connected to obtain DC output signals as depicted in Figure 10a. The

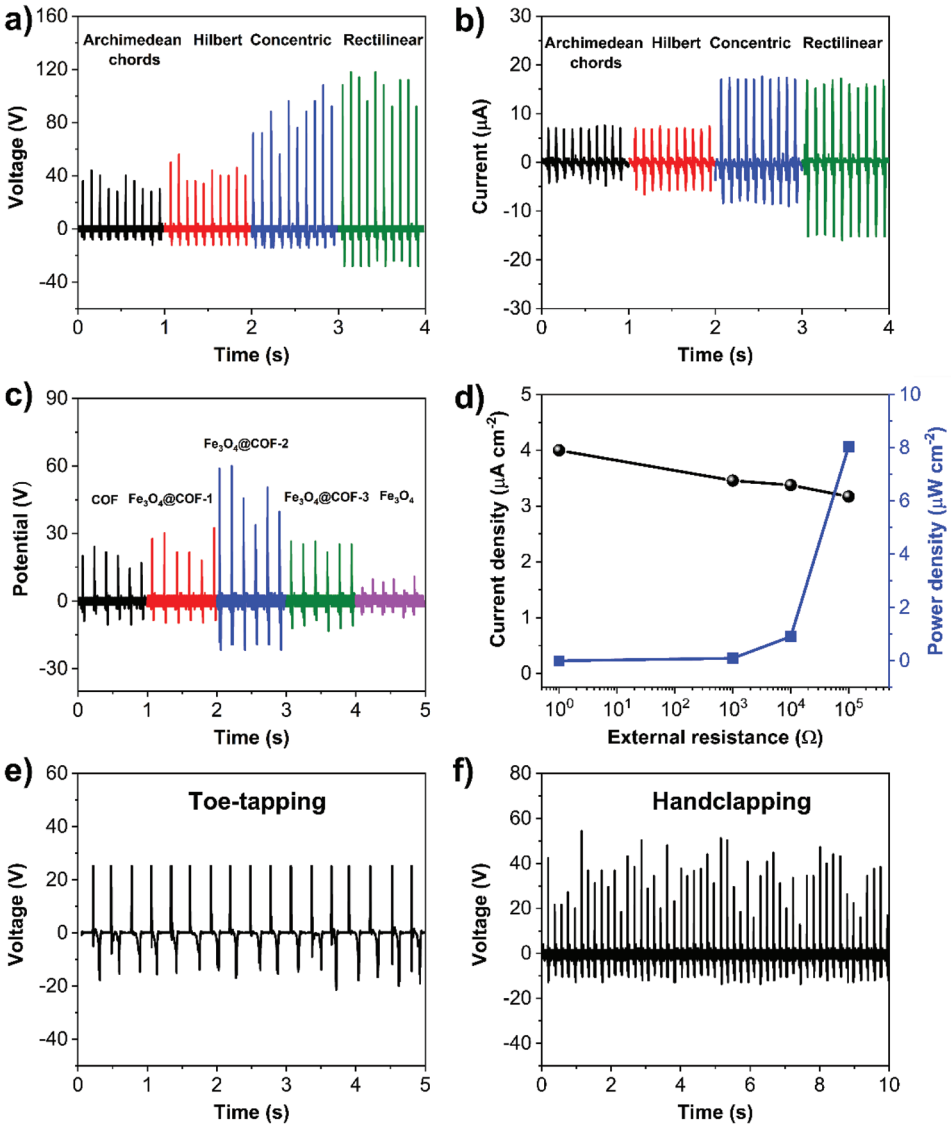

Figure 9. Variation of a) open-circuit voltage (V_{oc}) and b) short-circuit current (I_{sc}) with different engraved patterns on PDMS/MXene films, c) comparison of V_{oc} of CS-TENG for bare COF and Fe_3O_4 with Fe_3O_4@COF-1, Fe_3O_4@COF-2, and Fe_3O_4@COF-3 at contact frequency of 6 Hz, d) variation of power density with external resistance at contact frequency = 10 Hz, contact force = 2.8 N, e) V_{oc} recorded on human e) toe-tapping and f) handclapping modes.

negative end of the rectified circuit was connected to the Pt microelectrode thus acting as a cathode for HER, and the positive end of the rectified circuit was connected to a second Pt microelectrode that acted as anode for OER. The UME was positioned 8.8 μm above the center of the microelectrode to record the chronoamperometry data. The chronoamperograms for the HER and OER with different contact frequencies of the CS-TENG are shown in Figures 10b,e, respectively. The detected current intensities at UME for both HER and OER increased with increasing contact frequency from 6 to 10 Hz because the output voltage and current increased (compare Figure 8c,e). The magnified current responses for both the HER and OER are depicted in Figures 10c,f, respectively. The HER detection showed high peak currents of up to 320 nA at 10 Hz of contact frequency indicating an effective generation of hydrogen. The SECM images for the HER and OER at the substrate with a constant oscillation frequency of 8 Hz are shown in Figures 10d,g, respectively. The images demonstrate that the water splitting occurs localized at the substrate. The increasing current intensities at the center of the Pt electrode in Figure 10d,g affirm the evolution of a higher amount of H_2 and O_2 at the center of the electrode. An SECM image of the substrate showing the background signal without CS-TENG power is shown in Figure S7, Supporting Information.

2.5. Conversion of Biomechanical Energy to Chemical Energy

The experimental setup was modified to demonstrate that ambient mechanical energy from human body movement can

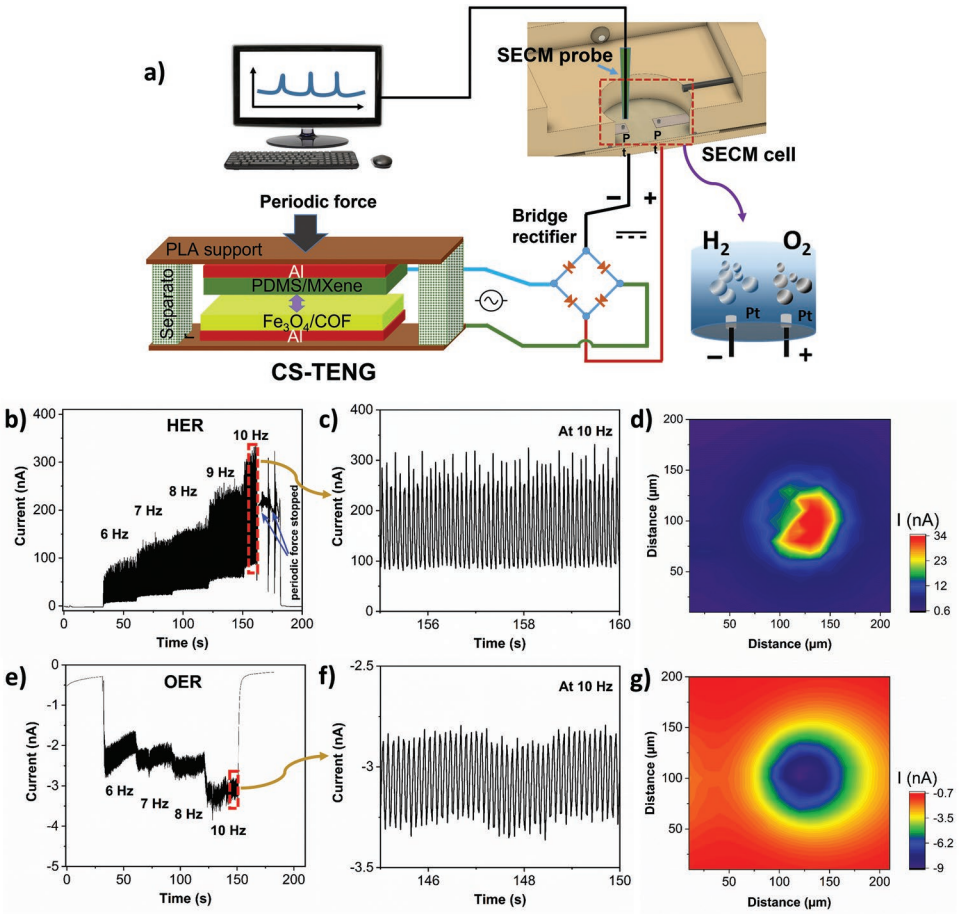

Figure 10. Electrochemical characterization of the mechanical to chemical energy conversion via water splitting. Schematic representation of the a) experimental setup: connection of the CS-TENG device with the SECM for hydrogen and oxygen generation. Chronoamperograms for b,c) hydrogen evolution reaction (HER) and e,f) oxygen evolution reaction (OER), and SECM images for d) HER and g) OER powered by the CS-TENG at a contact frequency of 8 Hz (electrolyte: 0.5 M H_2SO_4; E_{probe} = 0.05 V).

be converted to chemical energy. The handclapping mode was preferred to show an illustration of low-frequency movement that can generate green chemical energy. The CS-TENG device was placed on a person's hand to enable contact between two layers via handclapping. The continuous clapping on the CS-TENG to convert the mechanical energy into chemical energy is shown in Video S5, Supporting Information. The corresponding recorded chronoamperometric signal for HER is shown in **Figure 11**a. It is distinctly visible that clapping on the CS-TENG generates hydrogen in a pulsating manner. The chronoamperometric recording for the oxygen generation from the similar experiment is shown in Figure 11b. For both HER and OER, we observed no current response when clapping was stopped. The SECM images for the HER and OER from continuous clapping on the CS-TENG are shown in Figures 11c,d, respectively. The signal distribution and intensity show that hydrogen and oxygen production is similar while the CS-TENG was controlled by the linear actuator. However, the signal intensities are different and not uniform during manual operation as irregular frequency and associated force of hand clapping. In conclusion, the electrochemical investigation confirms the generation of hydrogen and oxygen from both, machine-controlled and human-body movement-based contact frequency. This demonstrates the successful application of CS-TENG for the direct conversion and storage of low-scale mechanical energy in chemical energy via water splitting.

3. Conclusions

Herein, we have shown that magnetic covalent organic framework composite (Fe_3O_4@COFs) can be used as potential positive triboelectric material and $Ti_3C_2T_x$ MXene-based PDMS composite film as negative triboelectric material for a contact-separation mode TENG. The amount of Fe_3O_4 content in the Fe_3O_4@COFs influence the electrical output. The Fe_3O_4@COF-2 shows approximately twofold higher performance than the bare COF. As Fe_3O_4@COF-2 has not been explored previously, it will make a position in the triboelectric series through this study. On the other hand, it has been found that 5 wt% of $Ti_3C_2T_x$ in PDMS gives the highest performance as a negative triboelectric material. As the $Ti_3C_2T_x$ possesses the surface terminals of electronegative elements −F, −OH that increase the negative surface charge density of the PDMS/MXene triboelectric

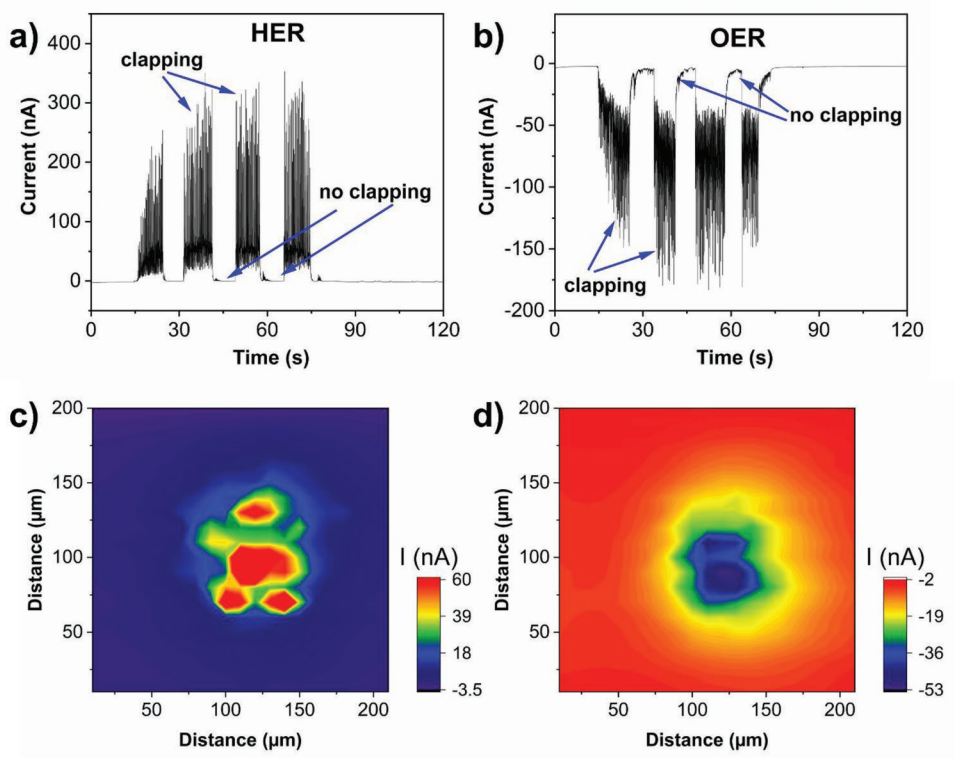

Figure 11. Characterization for the conversion of mechanical energy from handclapping to chemical energy. Chronoamperograms of the a) hydrogen evolution reaction (HER) and b) oxygen evolution reaction (OER), and SECM images of the c) HER and d) OER with continuous clapping by a person (electrolyte: 0.5 M H_2SO_4; E_{probe} = 0.05 V).

layer. Moreover, among the 3D-printed imprinted patterns of concentric, rectilinear, Hilbert, and Archimedean chords, the rectilinear pattern shows the highest performance. The CS-TENG generates a peak-to-peak open-circuit potential ($V_{oc(pk\text{-}pk)}$) of 146 V and a short-circuit current ($I_{sc(pk\text{-}pk)}$) of 32 μA at the contact frequency of 10 Hz with an applied contact force of 2.8 N. The alternate electric signals are rectified to direct current signals that are used for the electrolysis of water. The SECM measurement in substrate-generation/tip-collection and imaging modes confirms the H_2 and O_2 evolution. The electrolysis can be done using even small-scale mechanical energy such as hand clapping. Thus, such proof-of-concept for green hydrogen production can be extended to energy conversion from other renewable sources of mechanical energy like raindrops, streams, wind, sea waves, and even moving vehicles and trains. This work will show the future direction of harvesting green hydrogen everywhere with less dependence on other energy sources such as solar and wind turbines. Such conversion of renewable mechanical energy into green hydrogen will lead us to a "green zero carbon emission" in future decades.

4. Experimental Section

Materials: Magnetite (Fe_3O_4), 1,3,5-tris(p-formylphenyl)benzene, 4,4″-diamino-p-terphenyl, dimethyl sulfoxide (DMSO), potassium nitrate (KNO_3), acetic acid, and Nafion 117 solution were purchased from Merk, Germany and Ferrocene methanol (99%) was procured from ABCR GmbH, Germany. The SYLGARD 184 Silicone Elastomer Kit was bought from Dow, USA. Sulfuric acid (H_2SO_4) and tetrahydrofuran (THF) were purchased from Penta, Czech Republic. The PLA and polyethylene terephthalate glycol (PETG) filaments for 3D printing were purchased from Filament2Print, Spain. All the chemicals were of analytical grade.

Fabrication of MXene and PDMS/MXene Composite Films: The detailed synthesis of $Ti_3C_2T_x$ MXene is described in the previous report.[62,65] The PDMS film was fabricated by mixing the silicone elastomer solution and curing agent in a mass ratio of 10:1 of the commercial product SYLGARD 184. To prepare the PDMS/MXene composite film, MXene (3, 5, and 10 wt%) was mixed vigorously with the elastomer solution for 20 min. After that, the curing agent was added to it and stirred for another 10 min. The MXene/PDMS mixed solution was then poured into a 3D-printed PETG mold (width 20 mm, length 40 mm, and height- 0.2 mm) embedded with the 3D pattern on its surface as shown in Figure 1b. Four different patterns (concentric, rectilinear, Hilbert, and Archimedean chords) were selected from PrusaSlicer 2.4.2 software to design the mold's top surface. The PDMS/MXene solution after pouring into the mold kept in a vacuum for 12 h to remove the bubbles and afterward placed in an electric oven at 65 °C for 4 h to complete the curing process. The low-temperature curing process of PDMS was selected to prevent the distortion of PETG mold above its glass transition temperature (T_g). The PDMS/MXene films were peeled off from the molds carefully. Bare PDMS film was prepared following the same procedure without the addition of MXene as described above. The PDMS/MXene films with 0, 3, 5, and 10 wt% of MXene concentrations are denoted as bare PDMS, PDMS/MXene-3, PDMS/MXene-5, and PDMS/MXene-10, respectively.

Synthesis of the Covalent Organic Framework and Magnetic COF Composites (Fe_3O_4@COFs): The COF and Fe_3O_4@COFs were synthesized following a slightly modified procedure as previously reported in the literature.[55,66,67] At first, to synthesize the COF, 160 mg of 4,4″-diamino-p-terphenyl and 200 mg of 1,3,5-tris(p-formylphenyl)benzene were

mixed with 100 mL of DMSO in a round-bottomed flask and stirred for 5 min. After that, 4 mL of acetic acid was added to the mixture and heated at 75 °C for 30 min. The yielded yellowish product was vacuum filtered and washed with THF followed by ethanol several times to remove unreacted monomers. To synthesize the Fe_3O_4@COFs, a certain amount of Fe_3O_4 particles were added in the mixture of 4,4″-diamino-p-terphenyl and 1,3,5-tris(p-formylphenyl)benzene keeping monomers ratio and other parameters unaltered. The reaction yielded a yellowish-brown product that was separated by a magnet as shown in Video S1, Supporting Information, and was washed with THF and ethanol. The amount of Fe_3O_4 particles (100, 300, and 500 mg) was varied keeping the same monomer ratios, to yield three different Fe_3O_4@COFs. The Fe_3O_4@COFs with 100, 300, and 500 mg of Fe_3O_4 content are denoted as Fe_3O_4@COF-1, Fe_3O_4@COF-2, and Fe_3O_4@COF-3, respectively. The final products were dried in an electric oven at 60° for 6 h for the next use.

Materials Characterization: The morphology of the $Ti_3C_2T_x$ MXene, PDMS/MXene films, COF, Fe_3O_4, and Fe_3O_4@COFs were analyzed using SEM (FEI VERIOS 460L). The elemental mapping of the constituent elements of the samples was carried out with energy-dispersive X-ray spectroscopy using another SEM, Mira 3 XMU (Tescan) equipped with EDS (Oxford Instruments X-MAX) detector. The morphology of $Ti_3C_2T_x$ and Fe_3O_4@COF-2 were further characterized using TEM TITAN Themis 60–300 cubed (Thermofisher Scientific) using an accelerating voltage of 300 keV. The STEM imaging of Fe_3O_4@COF-2 was performed with bright-field and angular dark-field detectors. The STEM-EDX analysis of Fe_3O_4@COF-2 was carried out with a SUPER-X spectrometer (Thermofisher Scientific) with four 30 mm^2 windowless detectors. XPS was conducted to characterize and confirm the chemical composition of the COF and magnetic COF samples. The structural properties of COF, Fe_3O_4, and Fe_3O_4@COFs were examined via XRD analysis using a Rigaku SmartLab 3 kW X-ray diffractometer running at a voltage of 40 kV and a current of 30 mA. The Brag Brentano geometry analysis was followed maintaining Cu Kα radiation ($\lambda = 0.15418$ nm). The CLSM (Olympus Lext OLS4100) was used to obtain the optical and height profile images. A laser light source of a wavelength of 405 nm was used to operate the CLSM. The two-pass KPFM was carried out using Scanning Probe Microscope Bruker Dimension Icon (ICON-SPM) using a platinum-iridium coated tip of SCM-PIT-V2, Bruker. The topography was measured in the first-pass in tapping mode and the CPD was recorded in the second-pass. The Gwyddion software was used to process and analyze the KPFM data. A four-probe station (Cascade Microtech MPS 150) was employed to measure the electrical surface resistivity of the PDMS/MXene films. The 4-probe unit was connected to Keithley 4200-SCS Parameter Analyzer operated by Clarius software to record the data. 4-pt-resistivity-sweep of van der Pauw measurement was employed to measure the average resistivity.

Contact-Separation Mode Triboelectric Nanogenerator Device Fabrication and Electrical Output Measurement: The PDMS/MXene film (20 × 40 mm^2) was placed on the same size of Al foil (thickness 25 µm) keeping the patterned surface upside. A conductive Cu tape was connected to the Al foil to connect it to the oscilloscope probe terminal. The assembled PDMS/MXene-Al layer was fixed to a 3D-printed PLA substrate as the top plate. To fabricate the other triboelectric layer, the Fe_3O_4@COF particles were mixed with a binder Nafion 117 solution to make a slurry and coated on the Al foil (20 × 40 mm^2) following the doctor's blade technique to achieve a layer of 100 µm. Before coating the Fe_3O_4@COF slurry, the Al foil was pressed on a 3D-printed rectilinear patterned surface to imprint the pattern onto it to provide effective coating as shown in Figure S5a, Supporting Information. Afterward, the Fe_3O_4@COF/Al film was fixed with another 3D-printed PLA substrate to serve as the bottom plate. The top and bottom plates were then assembled placing two spacers (polyurethane foam) in between the PLA plates keeping a distance of 2 mm between the triboelectric layers. Further, to fabricate a flexible CS-TENG for generating electricity from biomechanical action, such as handclapping, the PDMS/MXene/Al and Fe_3O_4@COF/Al layers were attached with a piece of cotton cloths as supporting substrates instead of PLA.

The electrical measurement, such as V_{oc}, was recorded using a digital oscilloscope (GW Instek GDS-1074B) using a 10x probe, and the I_{sc} was measured using a custom-made I–V converter connected with the oscilloscope. An electric linear motor actuator with hub 20 mm (24 V DC, max 1000 rpm, DAOE) was used to hit on the CS-TENG's top plate to result in periodic contact at different actuation frequencies. The contact force was kept constant at 2.8 N for all cases. The tip of the oscilloscope probe was connected to the Fe_3O_4@COF/Al triboelectric layer and the ground lead was connected to the plate of the PDMS/MXene/Al layer. To convert the output AC signals to DC signals, a bridge rectifier (diode bridge, GM electronic) was connected to the CS-TENG terminals.

Scanning Electrochemical Microscopy Measurements: The SECM measurements were performed using an SECM, (Sensolytics, Germany) connected with an Autolab Bipotentiostat (PGSTAT302N, Metrohm, Netherlands). The SECM probe was a commercial Pt disc UME (Sensolytics, Germany) with a 25 µm electrode diameter and a tip-to-electrode ratio of 8. For the setup of electrolysis of water using the output voltage of TENG, the output terminals CS-TENG were connected with two Pt microelectrodes (generator electrodes) of 50 µm diameter. The Pt microelectrodes were fabricated by encapsulating two 50 µm Pt wires horizontally in 2-component epoxy resin using a vacuum impregnation chamber (CITOVAC, Struers Aps.) followed by curing and mechanical grinding/polishing (TEGRAMIN 30, Struers Aps.) to expose the end of the wires for electrolysis. Before water electrolysis experiments, the electrochemical cell was assembled and filled with a mediator solution containing 0.2 M KNO_3 and 1.5 mM Ferrocene methanol to position the SECM probe on the microelectrodes using the feedback mode ($E_{probe} = 0.4$ V). The tip-to-substrate distance was determined via probe approach curves[68] with an approach speed of 1 µm s^{-1} to be 13.8 µm for imaging and 8.8 µm for chronoamperometric experiments. All standard measurements were performed in a three-electrode setup using a graphite counter electrode, and an Ag/AgCl 3 M KCl as a reference electrode. After probe positioning, the electrolyte was exchanged with 0.5 M H_2SO_4 for electrolysis. The two generator microelectrodes were connected to the CS-TENG output terminals. The detection of the generated hydrogen or oxygen was recorded using the SG/TC mode with $E_{probe} = 0.05$ V. For the chronoamperometric detection, the measurement interval was 20 ms, resulting in 50 data points per second. Imaging experiments were carried out at constant height with a maximum scan speed of 100 µm s^{-1}, keeping a waiting time of 4 ms and a pixel size of 10 µm. Gwyddion 2.55 and OriginPro 2020 software were used for SECM data processing.

Supporting Information

Supporting Information is available from the Wiley Online Library or from the author.

Acknowledgements

K.G. and C.I. acknowledge the funding from the European Union's Horizon 2020 research and innovation program under the Marie Skłodowska-Curie grant agreement No (894457-MotionESt) and (888797-LoCatSpot), respectively. M.P. acknowledges the financial support by the Grant Agency of the Czech Republic (GACR EXPRO: 19–26896X). All authors thank the CzechNanoLab project LM2018110 at CEITEC Nano Research Infrastructure supported by MEYS CR for providing spectroscopic and microscopic characterization facilities. K.G. thanks Dr. Siowwoon Ng for reviewing the draft, Ms. Katarina Novčić for technical assistance with CLSM and SEM-EDX imaging, Ms. Aparna Vasudevan Kandathil for assisting in electrical sheet resistivity measurement, Dr. Mario Palacios Corella for assisting in FTIR measurement, Dr. Imrich Gablech for assisting in TENG setup, to Mr. Švarc Vojtěch for assembling the linear actuator motor, and to Dr. Mario Urso, Mr. Shidhin Mappoli, and Ms. Shaista Nouseen for assisting in shooting the videos.

Conflict of Interest

The authors declare no conflict of interest.

Author Contributions

K.G. conceptualized the project and synthesized the materials and characterized the structural and morphological analysis and electrical output of the triboelectric nanogenerator. C.I. fabricated and assembled the electrochemical cell, and measured and analyzed the scanning electrochemical microscopy for the electrolysis of water. M.K. performed the Kelvin probe force microscopy measurements and analyzed contact potential difference images. J.V. set up the *I–V* converter and guided the electrical output analysis. J.M. performed and analyzed results of TEM imaging and STEM-EDX spectroscopy. M.P. supervised the project. All authors contributed to the writing.

Data Availability Statement

The data that support the findings of this study are available from the corresponding author upon reasonable request.

Keywords

green hydrogen, magnetic COFs, mechanical energy conversion, MXene, renewable energy, triboelectric nanogenerators

Received: October 14, 2022
Revised: December 18, 2022
Published online: February 12, 2023

[1] J. Chang, M. Dommer, C. Chang, L. Lin, *Nano Energy* **2012**, *1*, 356.
[2] B. Kumar, S.-W. Kim, *Nano Energy* **2012**, *1*, 342.
[3] J. Chen, Y. Huang, N. Zhang, H. Zou, R. Liu, C. Tao, X. Fan, Z. L. Wang, *Nat. Energy* **2016**, *1*, 16138.
[4] K. Kendall, *Clean Technol.* **2022**, *4*, 345.
[5] Y. Chen, K. Yang, B. Jiang, J. Li, M. Zeng, L. Fu, *J. Mater. Chem. A* **2017**, *5*, 8187.
[6] F.-R. Fan, Z.-Q. Tian, Z. L. Wang, *Nano Energy* **2012**, *1*, 328.
[7] B. Shi, Z. Liu, Q. Zheng, J. Meng, H. Ouyang, Y. Zou, D. Jiang, X. Qu, M. Yu, L. Zhao, *ACS Nano* **2019**, *13*, 6017.
[8] X.-S. Zhang, M. Han, B. Kim, J.-F. Bao, J. Brugger, H. Zhang, *Nano Energy* **2018**, *47*, 410.
[9] J. Xiong, M. Lin, J. Wang, S. L. Gaw, K. Parida, P. S. Lee, *Adv. Energy Mater.* **2017**, *7*, 1701243.
[10] X. Cheng, B. Meng, X. Zhang, M. Han, Z. Su, H. Zhang, *Nano Energy* **2015**, *12*, 19.
[11] S. K. Karan, S. Maiti, J. H. Lee, Y. K. Mishra, B. B. Khatua, J. K. Kim, *Adv. Funct. Mater.* **2020**, *30*, 2004446.
[12] W. Tang, Y. Han, C. B. Han, C. Z. Gao, X. Cao, Z. L. Wang, *Adv. Mater.* **2015**, *27*, 272.
[13] X. Ren, H. Fan, C. Wang, J. Ma, H. Li, M. Zhang, S. Lei, W. Wang, *Nano Energy* **2018**, *50*, 562.
[14] G. Khandelwal, N. P. M. J. Raj, S. Kim, *Adv. Energy Mater.* **2021**, *11*, 2101170.
[15] E. Jin, M. Asada, Q. Xu, S. Dalapati, M. A. Addicoat, M. A. Brady, H. Xu, T. Nakamura, T. Heine, Q. Chen, *Science* **2017**, *357*, 673.
[16] B. Zhang, M. Wei, H. Mao, X. Pei, S. A. Alshmimri, J. A. Reimer, O. M. Yaghi, *J. Am. Chem. Soc.* **2018**, *140*, 12715.
[17] B. Bai, D. Wang, L.-J. Wan, *Bull. Chem. Soc. Jpn.* **2021**, *94*, 1090.
[18] C. Wang, Z. Zhang, Y. Zhu, C. Yang, J. Wu, W. Hu, *Adv. Mater.* **2022**, *34*, 2102290.
[19] L. Zhai, N. Huang, H. Xu, Q. Chen, D. Jiang, *Chem. Commun.* **2017**, *53*, 4242.
[20] Q. Sun, C.-W. Fu, B. Aguila, J. Perman, S. Wang, H.-Y. Huang, F.-S. Xiao, S. Ma, *J. Am. Chem. Soc.* **2018**, *140*, 984.
[21] C. Yuan, X. Wu, R. Gao, X. Han, Y. Liu, Y. Long, Y. Cui, *J. Am. Chem. Soc.* **2019**, *141*, 20187.
[22] C. S. Diercks, O. M. Yaghi, *Science* **2017**, *355*, eaal1585.
[23] E. Jin, Z. Lan, Q. Jiang, K. Geng, G. Li, X. Wang, D. Jiang, *Chem* **2019**, *5*, 1632.
[24] Z. Xie, B. Wang, Z. Yang, X. Yang, X. Yu, G. Xing, Y. Zhang, L. Chen, *Angew. Chem., Int. Ed.* **2019**, *58*, 15742.
[25] S. Xu, G. Wang, B. P. Biswal, M. Addicoat, S. Paasch, W. Sheng, X. Zhuang, E. Brunner, T. Heine, R. Berger, *Angew. Chem., Int. Ed.* **2019**, *131*, 859.
[26] A. Halder, M. Ghosh, A. Khayum M, S. Bera, M. Addicoat, H. S. Sasmal, S. Karak, S. Kurungot, R. Banerjee, *J. Am. Chem. Soc.* **2018**, *140*, 10941.
[27] G. Khandelwal, N. P. M. J. Raj, S. Kim, *Adv. Funct. Mater.* **2020**, *30*, 1910162.
[28] G. Khandelwal, N. P. M. J. Raj, S.-J. Kim, *J. Mater. Chem. A* **2020**, *8*, 17817.
[29] L. Zhai, W. Wei, B. Ma, W. Ye, J. Wang, W. Chen, X. Yang, S. Cui, Z. Wu, C. Soutis, *ACS Mater. Lett.* **2020**, *2*, 1691.
[30] Y. Hu, N. Dunlap, S. Wan, S. Lu, S. Huang, I. Sellinger, M. Ortiz, Y. Jin, S. Lee, W. Zhang, *J. Am. Chem. Soc.* **2019**, *141*, 7518.
[31] H. Zou, Y. Zhang, L. Guo, P. Wang, X. He, G. Dai, H. Zheng, C. Chen, A. C. Wang, C. Xu, Z. L. Wang, *Nat. Commun.* **2019**, *10*, 1427.
[32] C. Wu, T. W. Kim, J. H. Park, H. An, J. Shao, X. Chen, Z. L. Wang, *ACS Nano* **2017**, *11*, 8356.
[33] W. Seung, H. Yoon, T. Y. Kim, H. Ryu, J. Kim, J. Lee, J. H. Lee, S. Kim, Y. K. Park, Y. J. Park, *Adv. Energy Mater.* **2017**, *7*, 1600988.
[34] Y.-W. Cai, X.-N. Zhang, G.-G. Wang, G.-Z. Li, D.-Q. Zhao, N. Sun, F. Li, H.-Y. Zhang, J.-C. Han, Y. Yang, *Nano Energy* **2021**, *81*, 105663.
[35] W. Cao, H. Ouyang, W. Xin, S. Chao, C. Ma, Z. Li, F. Chen, M. Ma, *Adv. Funct. Mater.* **2020**, *30*, 2004181.
[36] W. He, M. Sohn, R. Ma, D. J. Kang, *Nano Energy* **2020**, *78*, 105383.
[37] D. Wang, Y. Lin, D. Hu, P. Jiang, X. Huang, *Composites, Part A* **2020**, *130*, 105754.
[38] X. Xia, J. Chen, G. Liu, M. S. Javed, X. Wang, C. Hu, *Carbon N Y* **2017**, *111*, 569.
[39] B. Anasori, M. R. Lukatskaya, Y. Gogotsi, *Nat. Rev. Mater.* **2017**, *2*, 16098.
[40] M. Naguib, V. N. Mochalin, M. W. Barsoum, Y. Gogotsi, *Adv. Mater.* **2014**, *26*, 992.
[41] M. R. Lukatskaya, S. Kota, Z. Lin, M.-Q. Zhao, N. Shpigel, M. D. Levi, J. Halim, P.-L. Taberna, M. W. Barsoum, P. Simon, *Nat. Energy* **2017**, *2*, 17105.
[42] M. Zhao, X. Xie, C. E. Ren, T. Makaryan, B. Anasori, G. Wang, Y. Gogotsi, *Adv. Mater.* **2017**, *29*, 1702410.
[43] C. Zhang, M. P. Kremer, A. Seral-Ascaso, S. Park, N. McEvoy, B. Anasori, Y. Gogotsi, V. Nicolosi, *Adv. Funct. Mater.* **2018**, *28*, 1705506.
[44] S. J. Kim, H.-J. Koh, C. E. Ren, O. Kwon, K. Maleski, S.-Y. Cho, B. Anasori, C.-K. Kim, Y.-K. Choi, J. Kim, *ACS Nano* **2018**, *12*, 986.
[45] S. Zhao, H.-B. Zhang, J.-Q. Luo, Q.-W. Wang, B. Xu, S. Hong, Z.-Z. Yu, *ACS Nano* **2018**, *12*, 11193.
[46] Q. Wang, H. Zhang, J. Liu, S. Zhao, X. Xie, L. Liu, R. Yang, N. Koratkar, Z. Yu, *Adv. Funct. Mater.* **2019**, *29*, 1806819.
[47] R. D. Farahani, M. Dubé, D. Therriault, *Adv. Mater.* **2016**, *28*, 5794.
[48] K. Ariga, *Nanoscale Horiz.* **2021**, *6*, 364.
[49] J. Izquierdo, P. Knittel, C. Kranz, *Anal. Bioanal. Chem.* **2018**, *410*, 307.

[50] D. Polcari, P. Dauphin-Ducharme, J. Mauzeroll, *Chem. Rev.* **2016**, *116*, 13234.
[51] G. Caniglia, C. Kranz, *Anal. Bioanal. Chem.* **2020**, *412*, 6133.
[52] A. Preet, T. E. Lin, *Catalysts* **2021**, *11*, 594.
[53] M. Zhang, R. Zheng, Y. Ma, R. Chen, X. Sun, X. Sun, *Molecules* **2019**, *24*, 3361.
[54] J. Huo, B. Luo, Y. Chen, *ACS Omega* **2019**, *4*, 22504.
[55] M. Wang, M. Gao, K. Zhang, L. Wang, W. Wang, Q. Fu, Z. Xia, D. Gao, *Microchim. Acta* **2019**, *186*, 827.
[56] H. Zou, L. Guo, H. Xue, Y. Zhang, X. Shen, X. Liu, P. Wang, X. He, G. Dai, P. Jiang, H. Zheng, B. Zhang, C. Xu, Z. L. Wang, *Nat. Commun.* **2020**, *11*, 2093.
[57] W. Melitz, J. Shen, A. C. Kummel, S. Lee, *Surf. Sci. Rep.* **2011**, *66*, 1.
[58] B. N. Reddy, P. N. Kumar, M. Deepa, *ChemPhysChem* **2015**, *16*, 377.
[59] M. Fonin, R. Pentcheva, Y. S. Dedkov, M. Sperlich, D. V. Vyalikh, M. Scheffler, U. Rüdiger, G. Güntherodt, *Phys. Rev. B* **2005**, *72*, 104436.
[60] B. Song, X. Wang, B. Li, L. Zhang, Z. Lv, Y. Zhang, Y. Wang, J. Tang, P. Xu, B. Li, *Opt. Express* **2016**, *24*, 23755.
[61] G. Z. Li, G. G. Wang, D. M. Ye, X. W. Zhang, Z. Q. Lin, H. L. Zhou, F. Li, B. L. Wang, J. C. Han, *Adv. Electron. Mater.* **2019**, *5*, 1800846.
[62] K. Ghosh, M. Pumera, *Small Methods* **2021**, *5*, 2100451.
[63] B. Yang, W. Zeng, Z. Peng, S. Liu, K. Chen, X. Tao, *Adv. Energy Mater.* **2016**, *6*, 1600505.
[64] A. J. Bard, M. V. Mirkin, *Scanning Electrochemical Microscopy*, 2nd ed., CRC Press, Boca Raton, FL **2012**.
[65] J. Vyskočil, C. C. Mayorga-Martinez, K. Szőkölová, A. Dash, J. Gonzalez-Julian, Z. Sofer, M. Pumera, *ChemElectroChem* **2019**, *6*, 3982.
[66] N. Li, D. Wu, J. Liu, N. Hu, X. Shi, C. Dai, Z. Sun, Y. Suo, G. Li, Y. Wu, *Microchem. J.* **2018**, *143*, 350.
[67] L. Wang, W. Gao, S. Ng, M. Pumera, *Anal. Chem.* **2021**, *93*, 5277.
[68] C. Lefrou, R. Cornut, *ChemPhysChem* **2010**, *11*, 547.